ADVANCED ENERGY MATERIALS
www.advenergymat.de

Understanding the Role of Order in Y-Series Non-Fullerene Solar Cells to Realize High Open-Circuit Voltages

*Lorena Perdigón-Toro, Le Quang Phuong, Fabian Eller, Guillaume Freychet, Elifnaz Saglamkaya, Jafar I. Khan, Qingya Wei, Stefan Zeiske, Daniel Kroh, Stefan Wedler, Anna Köhler, Ardalan Armin, Frédéric Laquai, Eva M. Herzig, Yingping Zou, Safa Shoaee, and Dieter Neher**

Non-fullerene acceptors (NFAs) as used in state-of-the-art organic solar cells feature highly crystalline layers that go along with low energetic disorder. Here, the crucial role of energetic disorder in blends of the donor polymer PM6 with two Y-series NFAs, Y6, and N4 is studied. By performing temperature-dependent charge transport and recombination studies, a consistent picture of the shape of the density of state distributions for free charges in the two blends is developed, allowing an analytical description of the dependence of the open-circuit voltage V_{OC} on temperature and illumination intensity. Disorder is found to influence the value of the V_{OC} at room temperature, but also its progression with temperature. Here, the PM6:Y6 blend benefits substantially from its narrower state distributions. The analysis also shows that the energy of the equilibrated free charge population is well below the energy of the NFA singlet excitons for both blends and possibly below the energy of the populated charge transfer manifold, indicating a down-hill driving force for free charge formation. It is concluded that energetic disorder of charge-separated states has to be considered in the analysis of the photovoltaic properties, even for the more ordered PM6:Y6 blend.

1. Introduction

Organic solar cells (OSCs) stand out because of their easy processability, flexibility, light weight, and the abundance of materials that can act as electron donor (D) or acceptor (A) in the active layer of such devices. Great efforts are put into the development of even a larger library of materials, and the appearance of new non-fullerene acceptors (NFAs) has injected new life into the technology.[1] Highest efficiencies are reported for single junction of ternary blends in which one of the components is the NFA Y6, or one of its close derivatives.[2–6] When blended with the polymer donor PM6, PM6:Y6 devices have high and reproducible power conversion efficiencies (PCEs), thus many studies have focused on elucidating what makes this blend so special.[7] Free charge generation was shown to be essentially

L. Perdigón-Toro, D. Neher
Soft Matter Physics and Optoelectronics
Institute of Physics and Astronomy
University of Potsdam
Karl-Liebknecht-Str. 24–25, 14476 Potsdam-Golm, Germany
E-mail: neher@uni-potsdam.de

L. Perdigón-Toro, L. Q. Phuong, E. Saglamkaya, S. Shoaee
Disordered Semiconductor Optoelectronics, Institute of Physics and Astronomy
University of Potsdam
Karl-Liebknecht-Str. 24–25, 14476 Potsdam-Golm, Germany

F. Eller, E. M. Herzig
Physikalisches Institut
Dynamik und Strukturbildung – Herzig Group
Universität Bayreuth
Universitätsstr. 30, 95447 Bayreuth, Germany

The ORCID identification number(s) for the author(s) of this article can be found under https://doi.org/10.1002/aenm.202103422.

DOI: 10.1002/aenm.202103422

G. Freychet
NSLS-II
Brookhaven National Laboratory
Upton, NY 11973, USA

J. I. Khan, F. Laquai
KAUST Solar Center (KSC)
Physical Sciences and Engineering Division (PSE)
King Abdullah University of Science and Technology (KAUST)
Thuwal 23955-6900, Kingdom of Saudi Arabia

Q. Wei, Y. Zou
College of Chemistry and Chemical Engineering
Central South University
Changsha 410083, P. R. China

S. Zeiske, A. Armin
Sustainable Advanced Materials (Sêr SAM)
Department of Physics
Swansea University
Singleton Park, Swansea SA2 8PP, UK

D. Kroh, S. Wedler, A. Köhler
Soft Matter Optoelectronics
Bayreuth Institut of Macromolecular Research (BIMF)
and Bavarian Polymer Institute (BPI)
University of Bayreuth
95440 Bayreuth, Germany

barrierless which was attributed to the molecular structure of Y6 and its large quadrupole moment, which causes band bending across the heterojunction and drives charge separation.[8] The unique molecular packing of Y6 has also been pointed out as responsible for electron delocalization at the D:A interface and consequent charge separation.[9] In comparison to NFAs reported earlier, neat films of Y6 have more preferential face-on orientation,[7,10,11] and clusters of Y6 are better connected, promoting faster transport of electrons, holes, and excitons.[12] Despite a favorable morphology, the PM6:Y6 blend lags in terms of charge extraction,[13] given its fairly high bimolecular recombination coefficient and moderate mobility.[8,14,15] Both properties are known to be related to the energetic disorder of the charge transporting states.[16–19] In addition, energetic disorder will reduce the open-circuit voltage (V_{OC}) because carriers accumulate in the tail of the electronic density of states (DOS).[20–22] Therefore, detailed knowledge of the interplay between energetic disorder and the physical processes determining the photovoltaic response is needed.

Compared to inorganics, organic semiconductors have a larger positional and energetic disorder. In bulk heterojunction (BHJ) solar cells, this is primarily a result of molecular and interfacial interactions and the multiple possible morphologies upon mixing of the donor and acceptor. Research spanning over a decade attempted to link energetic disorder to the photovoltaic parameters of polymer:fullerene OSCs.[20,22–29] Fullerene-based blends have large energetic disorder with values that can even exceed 100 meV.[30–33] This is because of the small aggregate size of substituted fullerenes such as PCBM ([6,6]-phenyl-C_{61}-butyric acid methyl ester) but also the significant orientational and conformational disorder even within these ordered domains.[34–36] Modern NFAs as used in state-of-the-art OSCs exhibit layers with a well-defined intermolecular nanostructure.[10,11,37] For OSCs with Y-series acceptors, both the lowest unoccupied molecular orbital (LUMO) and the highest occupied molecular orbital (HOMO) exhibit energetic disorder values typically between 50 and 70 meV.[14,15,38,39] Often, the effect of energetic disorder is described through a Gaussian or exponential model of the density of states and the V_{OC} can be analytically derived from the splitting of the quasi-Fermi levels in each model, while considering whether recombination occurs between free charges via bound states to the ground state, or between free charges and traps.[20,25,40] The different mechanisms can be discerned experimentally by determining the recombination parameters from the V_{OC} dependence on carrier density (m-factor) and generation current (ideality factor, n_{id}), and the recombination current dependence on carrier density (recombination order δ), as detailed in Refs. [24,40]. So far, though, few experimental studies have tried to link energetic disorder to the V_{OC} losses, the V_{OC} dependence on temperature or the main recombination mechanism in NFA blends.[38,41,42] An approach frequently used in literature to determine the disorder is to measure the Urbach energy from the slope of the tail of the external quantum efficiency (EQE_{pv}) spectrum.[38,43,44] However, for a Gaussian disorder, this slope will always be equal to the thermal energy, independent of the width of the DOS, σ.[45] Very recently, Brus et al.[42] explained the V_{OC} as a function of temperature and light intensity for several polymer:NFA blends, using a combination of bimolecular and trap-assisted recombination in the bulk and at the surface. To take energetic disorder into account, the recombination rates were related to a temperature-dependent mobility according to the Gaussian disorder model.[16] This yielded values of σ between 46 and 70 meV, depending on the system. Thereby, the same disorder was assumed for the HOMO and the LUMO. As for work on the PM6:Y6 blend, information on the energetic disorder was derived from temperature-dependent space charge-limited currents (SCLC) measurements but no corresponding measurement of the V_{OC} in relation to disorder was performed.[15] Interestingly, V_{OC} as a function of temperature data reported so far reveals a charge transfer (CT) energy, E_{CT}, of ≈1.1 eV when extrapolated to 0 K,[8,46,47] which is less than 0.3 eV above qV_{OC}. This points to energetic disorder affecting the V_{OC} of PM6:Y6 solar cells, even at room temperature.

In this work, we highlight the role of energetic disorder in NFA solar cells, by comparing Y6 to a close derivative, namely, N4. Grazing-incidence wide-angle X-ray scattering (2D-GIWAXS) reveals distinct differences of the molecular orientation and order for the two acceptors blended with PM6, while temperature-dependent SCLC measurements show a significantly smaller energetic disorder in PM6:Y6. Temperature-dependent bias-assisted charge extraction (BACE) measurements reveal that the recombination mechanism is different in both blends. In PM6:Y6, recombination occurs between charges in a Gaussian HOMO DOS and a Gaussian LUMO DOS, both of narrow width, whereas the main recombination mechanism in PM6:N4 is of carriers in a broader Gaussian LUMO DOS recombining with carriers in a HOMO DOS with an exponential tail. As a consequence, the V_{OC} of PM6:N4 is considerably lower compared to PM6:Y6. The effect of disorder on the V_{OC} as a function of temperature is quantitatively described by analytical models considering the shape and disorder of the HOMO and LUMO site distributions. Because of the higher disorder, the CT emission is well discernible in electroluminescence (EL) at low temperatures in PM6:N4, which we assign to emission from lower-lying states in a broad DOS distribution, again consistent with the larger voltage loss of this blend. Finally, for a given generation rate, the free carrier density increases with decreasing temperature in both PM6:Y6 and PM6:N4. This contrasts the view that charge separation is temperature-assisted or entropy-driven. Instead, this finding supports the model that band bending in combination with energetic disorder provides a down-hill driving force for free charge formation.

2. Results

2.1. Device Characteristics

Since it is well established that PM6:Y6 has a desirable morphology and thereby low energetic disorder, we aimed at having an in-depth comparison with an alternative NFA that features a different molecular packing but has a similar molecular structure, that is, a Y-derivative. N4 is a small molecule acceptor that has an aromatic backbone identical to that of Y6 but different alkyl chains elongation, with 4th-position branching on the nitrogen atoms of the pyrrole motif of the backbone (instead of 2nd-position as in Y6, see

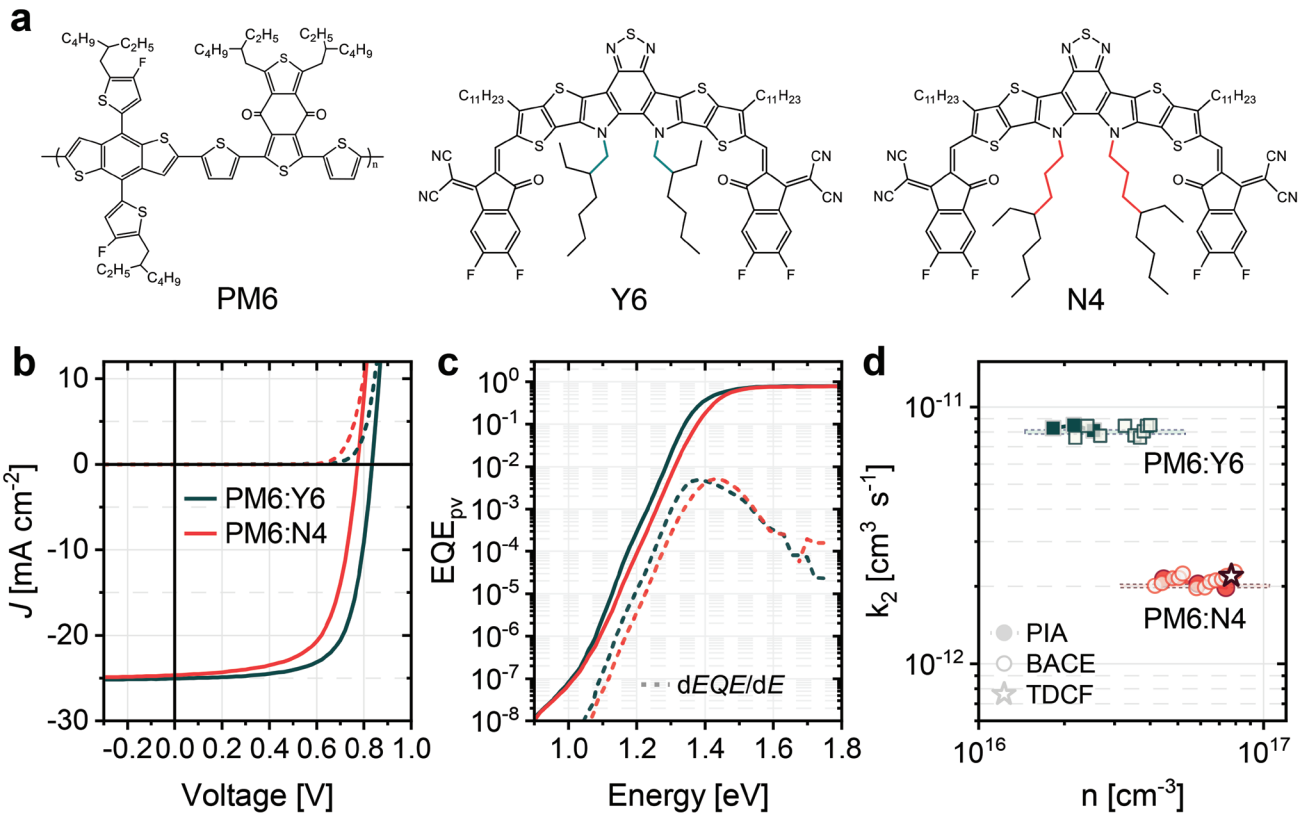

Figure 1. a) Chemical structures of PM6, Y6, and N4. b) Current density–voltage (*J–V*) characteristics of PM6:Y6 and PM6:N4 regular devices measured under simulated AM1.5G light (solid lines) and in the dark (dashed lines). c) Sensitive photovoltaic external quantum efficiency (s-EQE_{pv}) of PM6:Y6 and PM6:N4 devices (solid lines). The derivative d*EQE*/d*E* is shown in dashed lines and the photovoltaic gap E_G is determined from its maximum. The obtained E_G is 1.38 eV for PM6:Y6 and 1.43 eV for PM6:N4. d) Bimolecular recombination coefficient k_2 as a function of charge carrier density of PM6:Y6 and PM6:N4 devices measured via PIA (full symbols) and BACE (open symbols). For PM6:N4, the value of k_2 from TDCF-delay measurements is also plotted (star symbol).

Figure 1a). This increases the solubility of the N4 molecule.[48] Morphology studies performed by Jiang et al. showed that the PM6:N4 blend has a preferential *edge-on* orientation in contrast to the predominant *face-on* orientation of PM6:Y6. Moreover, R-SoXs experiments revealed larger but less pure domains in PM6:N4, pointing to more intermixing. As it turns out, the different molecular design and packing result in a poorer performance for the PM6:N4 devices, which have a lower V_{OC}, slightly lower fill factor (FF) but similar short-circuit current density (J_{SC}) when compared to PM6:Y6. The typical current density–voltage (*J–V*) characteristics of regular devices with a 100 nm layer of PM6:Y6 (1:1.2, wt%) and PM6:N4 (1:1.25, wt%) are shown in Figure 1b. Table S1 (Supporting Information) contains the averaged photovoltaic parameters of regular devices prepared in this work, while Figure S1 (Supporting Information) compares in more detail the statistics of both regular and inverted devices. Our regular PM6:Y6 devices exhibit a PCE average value of 14%, whereas the PCE of PM6:N4 is at 12%. Inspection of the photovoltaic parameters shows that the PM6:Y6 produces on average 1 mA cm^{-2} more in J_{SC} than the PM6:N4 (24.9 vs 23.9 mA cm^{-2}) for the same active layer thickness (Figure S2 shows the photovoltaic external quantum efficiency, EQE_{pv}, including the integrated J_{SC} for PM6:Y6 and PM6:N4, Supporting Information). In addition, the FF is 2% higher, with an average value of 66.8%, in PM6:Y6 compared to an average of 64.7% in PM6:N4. The largest difference is in the V_{OC}, which on average is 0.84 V in PM6:Y6 and 0.77 V in PM6:N4.

The large difference in V_{OC} comes as a surprise as N4 has been reported to have a slightly deeper HOMO and higher LUMO than Y6.[49] In accordance, the comparison in Figure 1c of the sensitive photovoltaic external quantum efficiency (s-EQE_{pv}) spectra shows that the absorption is blueshifted in PM6:N4 with respect to PM6:Y6. The same holds for the peak of the EQE derivative, which gives a photovoltaic gap of 1.38 and 1.43 eV for PM6:Y6 and PM6:N4, respectively. These results indicate that the PM6:N4 blend suffers overall from larger voltage losses. This is indeed observed in measurements of the external quantum efficiency of electroluminescence (ELQY), in Figure S3 (Supporting Information).

For a given energetics, a smaller V_{OC} would originate from faster geminate and/or nongeminate nonradiative recombination. Our previous measurements of time-delayed collection field (TDCF) on PM6:Y6 devices demonstrated that free charge generation is very efficient and independent of the electric field, pointing to small geminate losses in the blend. Similar results were obtained now for PM6:N4 (Figure S4, Supporting Information). We

investigated nongeminate recombination of regular PM6:Y6 and PM6:N4 devices with a semitransparent back electrode by means of charge extraction and optical-based spectroscopy techniques under steady-state conditions, namely bias assisted charge extraction (BACE) and quasisteady-state photoinduced absorption (PIA). In BACE, the device is held at V_{OC} under steady-state illumination and as soon as the light is turned off, a high reverse bias is applied to extract all charges.[50,51] Provided the recombination rate, R, follows a second order dependence on charge carrier density n, k_2 is directly calculated from $R = k_2 n^2$. PIA measurements are also performed at V_{OC}, but the yield and dynamics of free carriers are recorded by measuring the differential absorption upon modulation of the intensity of the quasi steady-state illumination.[52,53] Further experimental details on both techniques are given in the Supporting Information. The results from both methods point to second order recombination in the blends. The recombination coefficients as a function of carrier density are compared in Figure 1d, where we observe that $k_2 \approx 8 \times 10^{-12}$ cm^3 s^{-1} for PM6:Y6 and $k_2 \approx 2 \times 10^{-12}$ cm^3 s^{-1} for PM6:N4, meaning that recombination is ≈4 times slower in PM6:N4. This comes initially as a surprise since it is on the contrary a higher k_2 which would explain increased V_{OC} losses.[20,22] We note that the k_2 for the PM6:Y6 regular devices in this work is lower than in our previous report, which could be related to using a newer batch of the blend materials. To confirm the conclusions about the recombination loss in PM6:N4, we additionally performed transient recombination measurements with TDCF. TDCF has been already applied to PM6:Y6 and gave excellent agreement to BACE results.[54] The corresponding TDCF transients for PM6:N4 are shown in Figure S5 (Supporting Information). Analysis of these transients with an established model yielded the same k_2 as obtained via BACE and PIA, as marked in Figure 1d. A further source of V_{OC} losses is nonradiative recombination at the electrodes due to nonideal contacts. To rule out carrier losses due to surface recombination, we followed the same approach as for our PM6:Y6 devices,[55] and measured PIA and electromodulation injection-induced absorption (EMIA) spectroscopy on the same PM6:N4 device with regular architecture. These two complementary techniques allow us to compare photogenerated and dark injected charges at equivalent recombination currents (Figure S6, Supporting Information). At 1 sun, the carrier concentration under dark injection is slightly lower than under photoexcitation, but this would only cause a ≈15 meV difference in the quasi-Fermi level splitting (QFLS). Furthermore, we compared the photogenerated carrier concentration in a full device and a PM6:N4 bare film on glass (Figure S6, Supporting Information). Here, the PM6:N4 data on device and film agree very well, as was the case for PM6:Y6,[53] suggesting that little carriers are lost due to the incorporation of transport layers and electrodes (known as interfacial or surface recombination). Consequently, the reason for the lower V_{OC} of the PM6:N4 blend must lie in the details of the energetics and recombination mechanism in the bulk, which motivated a thorough study of the morphology and energetic disorder of the two blends and the resulting photovoltaic properties, as detailed in the following.

2.2. Morphology and Energetic Disorder

We employed grazing-incidence wide-angle X-ray scattering (2D-GIWAXS) to investigate the differences in the blend morphology of PM6:Y6 and PM6:N4 films. **Figure 2**a shows the 2D-GIWAXS images of PM6:Y6 and PM6:N4. In order to disentangle the contribution of the single components in the blend, we measured films of all neat materials. Figure 2b,c corresponds to the horizontal and vertical line cuts, respectively, of the neat materials PM6, Y6, and N4 (2D data can be found in Figure S7, Supporting Information), while Figure 2d,e contains the horizontal and vertical line cuts of the blends (from panel a). In Figure 2b,c, neat Y6 shows predominantly *face-on* orientation, as we observe the π–π stacking in the vertical direction while the lamellar peaks are identified in the horizontal direction, in line with previous reports.[7,10,11] The Gaussian peak shape (coherence length of 6.4 nm) of the first lamellar peak suggests long range order within the Y6 network. On the contrary, the π–π stacking in neat N4 is in the horizontal direction, pointing to preferential edge-on orientation. In addition, the lamellar stacking of N4 shows well defined, multiple structure peaks into specified directions which are more pronounced in comparison to the N4 π–π stacking signal. Thus, the lamellar stacking seems to be the more dominant stacking mechanism for neat N4. The length of the side-chain before the branching point could to be decisive in this competition, as a result of steric hindrance and/or the better solubility of N4.[56,57] Overall, neat N4 is highly ordered but, in comparison to neat Y6, the π–π stacking is less pronounced and the width of the peak is larger due to stronger cumulative disorder in the π–π stacking of N4. For the neat PM6, there is strong lamellar stacking in the vertical direction, i.e., edge-on preferential orientation, while there is only evidence of a very weak π–π stacking (Figure S7, Supporting Information). The corresponding data for the blends are shown in Figure 2a,d,e. For PM6:Y6, we notice that the first lamellar peak at $q_{xy} = 0.29$ Å^{-1} is contributed by both PM6 and Y6 (making it hard to distinguish them), but the second lamellar peak at $q_{xy} = 0.42$ Å^{-1} must have a Y6 contribution, meaning there is long range order of Y6 present within the blend. We attribute the π–π stacking in the vertical direction at $q_z = 1.7$ Å^{-1} almost solely to Y6 since the peak shape is nearly identical to the neat Y6 and PM6 has a weak π–π stacking. Conclusively, Y6 maintains its preferential face-on packing when blended with PM6 and spincoated from CF with 0.5% v/v CN. In PM6:N4, the N4 lamellar ordering ($q_{xy} = 0.33$ Å^{-1} and $q_{xy} = 0.41$ Å^{-1}) appears to have completely vanished, since the observed lamellar peaks in the blend resemble those of PM6 in position and shape. The lamellar peak at $q_{xy} = 0.29$ Å^{-1} of the PM6:N4 blend has a larger isotropic contribution than in the PM6:Y6 blend, i.e., PM6 is more isotropic, if blended with N4. Interestingly, the π–π stacking in the PM6:N4 blend is stronger in the vertical direction. It is unlikely that this signal is dominated by the PM6 which has a slightly preferred orientation of the lamellar stacking in the vertical. This in turn indicates that N4 is partially reoriented to face-on in our PM6:N4 blend. This contrasts with previous morphology studies,[48] where no significant π–π stacking could be observed for PM6:N4, while the lamellar stacking appeared to be similarly dominated by PM6 and thus no information on the N4 orientation in the blend

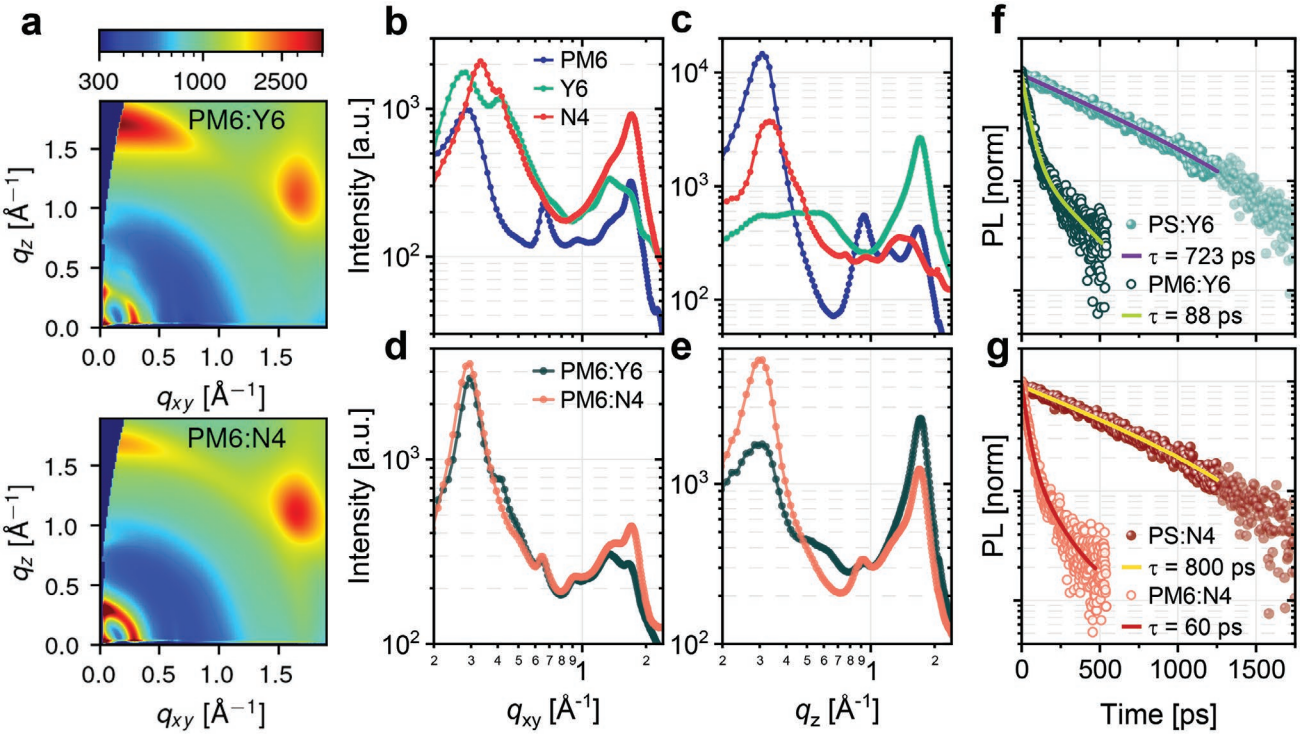

Figure 2. a) 2D-GIWAXS images of PM6:Y6 (top) and PM6:N4 (bottom) measured on Si substrates (the strong diffraction signal at about $q_{xy} = 1.7$ Å^{-1}, $q_z = 1.2$ Å^{-1} is due to substrate scattering). b) Horizontal and c) vertical line cuts of the neat materials PM6, Y6, and N4. d) Horizontal and e) vertical line cuts of the blends PM6:Y6 and PM6:N4. Time-resolved photoluminescence measured on f) PS:Y6 and PM6:Y6 films and g) PS:N4 and PM6:N4 films, from which a quenching efficiency of 88% and 93%, respectively, were determined.

could be obtained. This difference could be a result of using a different PM6 batch, with, e.g., different molecular weight and/or polydispersity, or slightly different processing conditions. In our blends, the addition of PM6 changes the environment of the N4 leading to a clearly altered aggregation behavior of the N4 including changes in the final orientation of the π–π stacking and a loss in regular nanostructure between N4 molecules. Taking a closer look at the π–π stacking, the intensity of the peaks is larger in PM6:Y6 compared to PM6:N4, meaning quantitatively that more NFA π–π stacking in *face-on* direction is present in our Y6 blend. We finally performed Pseudo-Voigt fits to the π–π peak and the disordered contribution in the vertical direction (see Figure S8, Supporting Information). The ratio between the area of π–π peak and amorphous contribution is ≈2.5 for PM6:N4 and ≈5.4 for PM6:Y6, revealing a larger amorphous fraction in the PM6:N4 blend in comparison to the PM6:Y6 in the π-π stacking direction. Thus, all the morphological features collected here indicate a lower degree and quality of stacking of N4 in the PM6:N4 blend in comparison to the neat N4 film, as well as in comparison to the Y6 in the PM6:Y6 blend. Here, stacking refers to the lamellar as well as the π-π stacking. Particularly in the vertical direction, it becomes apparent that the PM6:N4 blend shows less order than PM6:Y6 on the short length scales that are decisive for the electronic interactions of the materials.

We noted earlier that PM6:N4 has a lower domain purity.[48] To conveniently examine this, we measured time-resolved photoluminescence (TRPL) on films of the neat acceptors blended with the inert polymer polystyrene (PS) and on the blends with PM6, as shown in Figure 2f,g. The PS:NFA data are fitted using a single exponential decay, while the PM6:NFA blends are fitted using two exponentials, see Note S1 and Table S2 for details (Supporting Information). As expected, the blends with PM6 exhibit shorter lifetimes due to exciton quenching. In Figure 2f, the singlet exciton lifetime obtained for PS:Y6 is 723 ps and the weighted-average lifetime of PM6:Y6 is 88 ps, which gives a quenching efficiency of 88%. For the N4 blends, PS:N4 has a lifetime of 800 ps and PM6:N4 has 60 ps, thus the quenching efficiency is higher at 93%. Stronger exciton quenching is consistent with more intermixing in PM6:N4, i.e., more interfacial area between donor and acceptor. This in turn could be a potential source for a broadening of the DOS. For example, the presence of the other molecule disrupts the intermolecular order of the majority phase, going along with a larger energetic disorder. Also, all Y-series acceptor molecules exhibit quite large electrical dipole and quadrupole moments which, when mixed at low concentrations into PM6, could increase the energetic disorder in the donor phase.[58,59] In general, more intermixing will create larger D:A interfaces and a larger density of CT states, discerned by a broader and more significant low energy tail in EQE_{pv} measurements.[60,61] However, as we have previously shown for PM6:Y6,[55] the tail of the sensitive EQE_{pv} is dominated by the Y6 exciton and there is no discernible evidence for CT absorption. We concluded this by measuring the photoluminescence (PL) spectrum of the blend, which is largely dominated by emission from the Y6 singlet exciton and using the optoelectronic reciprocity by Rau[62] to calculate the EQE_{pv} spectrum due to exciton absorption. We performed the

Table 1. Energetic disorder parameters for the LUMO ($\sigma_{L,A}$) and the HOMO ($\sigma_{H,D}$), and zero-field electron (μ_e) and hole (μ_h) mobilities in the blends PM6:Y6 and PM6:N4.

Blend	$\sigma_{L,A}$[meV]	$\sigma_{H,D}$[meV]	μ_e[x10^{-4} cm^2 V^{-1} s^{-1}]	μ_h[x 10^{-4} cm^2 V^{-1} s^{-1}]
PM6:Y6	60	74	8.4	1.3
PM6:N4	66	90	1.6	0.1

same characterization for PM6:N4 in Figure S9 (Supporting Information), where we observe that emission and absorption are dominated by N4 singlets. The reciprocity of the PL perfectly reproduces the tail of the measured s-EQE$_{pv}$ except from ≈1.2 eV and below, which indeed indicates additional absorption due to a low energy CT population.

To establish the effect of the different morphologies on the energetic properties, we measured space charge limited currents (SCLC) of electron-only and hole-only devices as a function of temperature (see Note S2 and Figures S10–S11, Supporting Information). This approach has been shown to be sensitive to the shape and width of the DOS. We note that in order to avoid the effect of diffusion enhanced transport,[63] devices thicker than our typical solar cells were needed (typically larger than 150 nm). The temperature dependence of the zero-field mobility μ_0 for the PM6:Y6 and PM6:N4 blends is shown in Figure S12 (Supporting Information). **Table 1** summarizes the values of μ_0 at 300 K and the energetic disorders for the HOMO, $\sigma_{H,D}$, and the LUMO, $\sigma_{L,A}$, obtained using the Gaussian disorder model (GDM), see Note S2 (Supporting Information). When it comes to the LUMO, the disorder is slightly larger in PM6:N4, at 66 meV, while it is only 60 meV in the PM6:Y6. The electron mobility is then 5 times lower in PM6:N4 compared to PM6:Y6. It is in the HOMO where striking differences in disorder values are observed. The $\sigma_{H,D}$ increases from 74 meV in PM6:Y6 to 90 meV in PM6:N4, going along with a 10 times decrease of the zero-field mobility. It seems that the lower molecular order of PM6:N4 leads to a slight increase of disorder in the LUMO, while affecting to a greater extent the width of the HOMO DOS. From the earlier TRPL results, we speculate that N4 molecules mix into PM6 domains.

In addition, it becomes meaningful to plot the logarithmic slope of the *J*–*V* curves, slope = $d(\log J)/d(\log V)$, to reveal the SCLC regime and the presence of energetic traps.[16,64–66] This is done in Figures S10 and S11 (Supporting Information) in dependence of the applied voltage for PM6:Y6 and PM6:N4 electron- and hole-only devices. The electron-only devices of both blends follow a slope between 2 and 2.5 at higher voltages. The slight increase, especially at lower temperatures, is most likely due to a field-dependence of the mobility. The situation is the same for the PM6:Y6 hole-only data. The device that behaves differently is the hole-only PM6:N4. Here, the slope saturates at higher fields and the saturation value increases with decreasing temperature, reaching close to 4 at 223 K. This behavior is characteristic for an exponential distribution of tail states.[67,68] For SCLCs in a pure exponential DOS, $J \propto V^{2l+1}$, with $l = T_0/T$ and T_0 being the characteristic distribution temperature of the exponential DOS (see Note S3, Supporting Information). The best fit of the PM6:N4 hole-only data is shown in Figure S13 (Supporting Information) and yields T_0 = 585 K. The true width may, however, be smaller as this analysis does not consider an explicit voltage dependence of the free carrier mobility.

2.3. Nongeminate Recombination

The shape of the DOS does not only affect the free carrier transport but also its nongeminate recombination characteristics.[21,27,69–71] In brief, the recombination rate R is defined as the decay of charge carriers n with time, $R = -\frac{dn}{dt} = \gamma n^{\delta}$, where δ is the recombination order and γ the recombination coefficient. As introduced earlier, bimolecular recombination gives $\delta = 2$ and the recombination coefficient is then denoted as k_2. At V_{OC} conditions, recombination equals generation, while the generation rate G can be expressed in terms of the generation current J_G

$$J_G = qdR = qd\gamma n^{\delta} \tag{2a}$$

where q is the elementary charge and d is the film thickness. The steady-state recombination current is connected to the applied voltage, V, via the ideality factor, n_{id}, according to $J_R = J_0 \exp\left(\frac{qV}{n_{id}k_BT}\right)$, with J_0 being the dark recombination current, T temperature and k_B, the Boltzmann constant. Then, at open-circuit conditions

$$J_G(V_{OC}) = J_R(V_{OC}) = J_0 \exp\left(\frac{qV_{OC}}{n_{id}k_BT}\right) \tag{2b}$$

In absence of surface recombination, the V_{OC} is equal to the quasi-Fermi level splitting in the bulk which in turn, for equilibrated electrons and holes, is a function of the electron and hole densities, n and p. For an ideal intrinsic semiconductor with sharp bands, $n = p \propto \exp\left(\frac{qV_{OC}}{2k_BT}\right)$. In general, the relation between V_{OC} and n is written as

$$n = p = N_0 \exp\left(\frac{qV_{OC}}{2mk_BT}\right) \tag{2c}$$

where the *m*-factor is introduced to describe the degree of disorder and N_0 is the effective density of states. In case of two Gaussians, δ = 2, m = 1 and n_{id} = 1, with all parameters being independent of temperature.[40] We already note here that for a Gaussian DOS, these considerations are only correct in the nondegenerate limit (see Note S4, Supporting Information).[72] As we will show later, the approximation holds for $T \gtrsim 200\ K$ in the PM6:Y6 blend. In contrast, once an exponential DOS is involved in recombination, at least two of the above parameters depend on l, and with that on temperature,[40] given that $l = T_0/T$ as introduced earlier. Moreover, it makes a difference whether free or trapped carriers are involved. The reason is that for an exponential DOS the free carrier density is a nonlinear function of the total carrier density according to $n \propto (n_T)^l$.

Following Equation (2a–c), we measured *J*–*V*s and $n(V_{OC})$ at different illumination intensities and as a function of

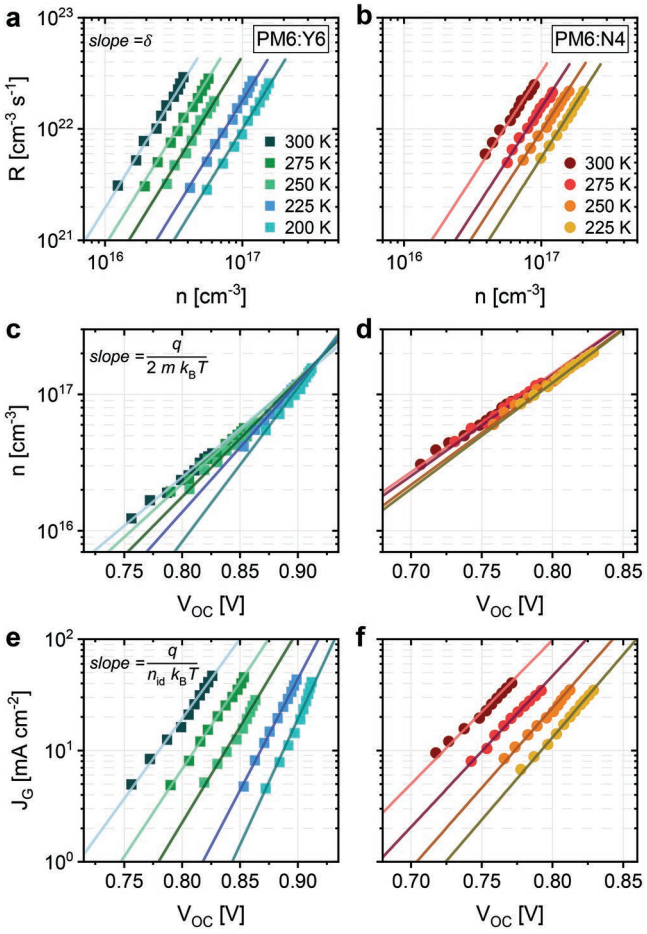

Figure 3. Recombination rate as a function of charge carrier density to determine the recombination order δ at different temperatures for a) PM6:Y6 and b) PM6:N4 devices. Charge carrier density as a function of V_{OC} to determine the *m*-factor at different temperatures for c) PM6:Y6 and d) PM6:N4 devices. Generation current density as a function of V_{OC} to determine the ideality factor n_{id} at different temperatures for e) PM6:Y6 and f) PM6:N4 devices. δ, the *m*-factor and n_{id} were extracted from the slope of the solid line fits (see equations in the left side panels).

temperature. **Figure 3**a,b shows the recombination rate *R* as a function of carrier density, measured using BACE, to determine δ for PM6:Y6 and PM6:N4. For both blends, we were able to fit the entire temperature range with a slope close to 2 (see the solid lines in the plots). We also notice that the recombination is slowed down at lower temperatures and the carrier density increases in both blends, which we will discuss in greater detail below. Differences between the blends appear in the charge carrier dependence on V_{OC} as shown in Figure 3c,d. While the slope of log (*n*) versus V_{OC} becomes larger with lower temperatures in the PM6:Y6 blend, it is nearly constant in PM6:N4. Remarkably, the PM6:N4 data points seem to merge onto one line, which is clearly not the case for PM6:Y6. The same effect is seen in the log (J_G) versus V_{OC} plots in Figure 3e,f where we observe a weak (if any) T-dependence of the slope for PM6:N4.

These findings are summarized in **Figure 4**a, where the parameters δ, *m* and n_{id} taken from the fits in Figure 3 are plotted as a function of temperature. The values of the recombination order δ assemble around 2 for both blends, with no appreciable dependence on temperature. As anticipated for the PM6:Y6 device, *m* and n_{id} remain constant at values of around 1.2 in the range of 300 K down to 200 K. The temperature independence and values close to 1 support the picture that the recombination of free carriers in PM6:Y6 involves mainly two Gaussians, as we reported before.[8] This situation is sketched in Figure 4b. A possible cause for n_{id} being slightly above one is additional recombination through midgap traps.[73] At 300 K, PM6:N4 has similar values of *m* and n_{id} as PM6:Y6, close to 1, but as the sample is cooled down, both parameters increase to above 1.4 at 225 K. According to Hofacker and Neher,[40] it is only when free charges in a Gaussian recombine with trapped charges in an exponential that the recombination order is equal to 2 and independent of temperature, but *m* and n_{id} depend on *T*. For this case, $n_{id} = m = \frac{1}{2}\left(1+\frac{T_0}{T}\right)$. This equation gives a reasonable fit to the experimental data (dashed gray line in Figure 4a), yielding T_0 = 435 K. We will discuss the discrepancy to the value from the T-dependent SCLC measurements below. According to SCLC results of PM6:N4 we assign a purely Gaussian shape to the density of electron-transporting states, while the density of hole-transporting states is characterized by an exponential tail (see Figure 4c for a schematic presentation of this situation). A possible scenario is that holes become immobilized in the exponential tail of the PM6 HOMO, while electrons move more freely in the Gaussian-shaped DOS of the N4 LUMO. Recombination takes place either at the interdiffused D:A heterojunction or electrons penetrate into the PM6-rich phase via dissolved N4 molecules. As mentioned above, R-SoXS revealed a smaller domain purity in the PM6:N4 blend compared to PM6:Y6, and GIWAXS showed no significant nanostructure between different N4 molecules when blended with PM6 apart from π–π stacking.

2.4. Predicting the Open-Circuit Voltage as a Function of Temperature

The models proposed in Figure 4b,c suggest that the two blends will differ in their quasi-Fermi level splitting, QFLS = $E_{F,e} - E_{F,h}$, and with that in their V_{OC} and its dependence on temperature and illumination intensity. For a Gaussian-type HOMO and LUMO, $E_{F,e} = E_{L,A} - \frac{\sigma_{L,A}^2}{2k_BT} + k_BT \ln\frac{n}{N_0}$ and $E_{F,h} = E_{H,D} + \frac{\sigma_{H,D}^2}{2k_BT} - k_BT \ln\frac{p}{N_0}$, with $E_{L,A}$ and $E_{H,D}$ being the center of the respective DOSs. Under the assumption that the electron and hole densities are equal ($n = p$) under illumination at open-circuit conditions, the V_{OC} can be described analytically as

$$q\,V_{OC} = E_{F,e} - E_{F,h} = E_g - \frac{\sigma_{L,A}^2 + \sigma_{H,D}^2}{2k_BT} + 2k_BT \ln\frac{n}{N_0} \quad (3a)$$

where $E_g = E_{L,A} - E_{H,D}$. As discussed in the Note S4 (Supporting Information), the above expression holds in the limit of an equilibrated population at high enough temperature, where the

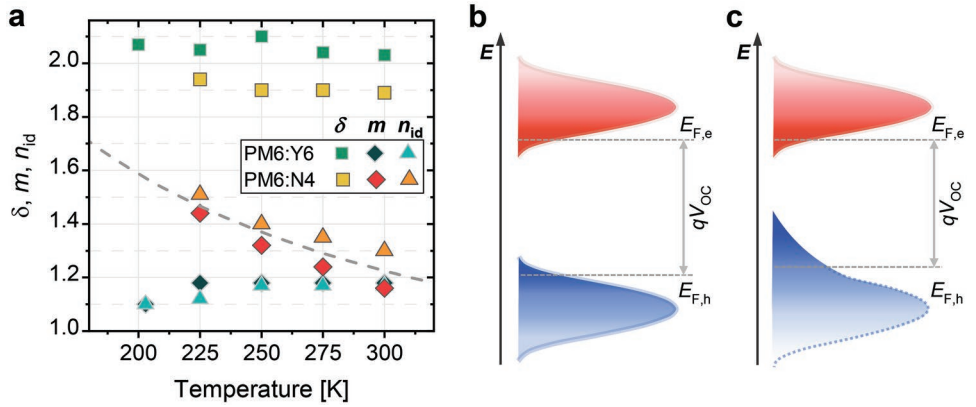

Figure 4. a) Dependencies of the parameters δ, the m-factor and n_{id} on temperature for PM6:Y6 and PM6:N4 devices. δ and the m-factor were obtained from temperature-dependent BACE and n_{id} from temperature-dependent J–Vs. The dashed line is a fit to the PM6:N4 data according to the equation $n_{id} = m = \frac{1}{2}\left(1+\frac{T_0}{T}\right)$, as predicted for free-trapped recombination in the Gaussian-exponential model. b) Scheme of HOMO and LUMO density distributions for a Gaussian–Gaussian model. c) Model of the HOMO and LUMO for PM6:N4, where recombination is dominated by holes in an exponential tail. $E_{F,e}$ and $E_{F,h}$ are the quasi-Fermi levels for electrons and holes, respectively.

state population can be described by a Boltzmann distribution. This is the case when the quasi-Fermi levels are more than $3k_BT$ away from the so-called equilibrium energies of the Gaussian DOSs. To predict the V_{OC} at low temperatures, the degenerate case has to be considered, for which Paasch et al.[72] provided an analytical approximation (Note S4 and Figure S14, Supporting Information).

In contrast, for holes in an exponential DOS, there is no distinction between non-degenerate and degenerate regions and $E_{F,h} \cong E_{H,D} - k_BT_0 \ln\frac{p}{N_0}$.[74] Then, assuming again $n = p$, the V_{OC} expression for the Gaussian-exponential model in the nondegenerate limit is

$$q\,V_{OC} = E_{F,e} - E_{F,h} = E_g - \frac{\sigma_{L,A}^2}{2k_BT} + k_B\,(T+T_0)\ln\frac{n}{N_0} \tag{3b}$$

See the Note S4 (Supporting Information) for the corresponding equation in the degenerate regime.

Equation (3a) predicts that for the combination of two Gaussians, the increase of V_{OC} with decreasing temperature due to the entropic contribution becomes partially compensated by the reduction of the effective bandgap, $E_g^{eff} = E_g - \frac{\sigma_{L,A}^2 + \sigma_{H,D}^2}{2k_BT}$, especially at low temperatures. For the Gaussian-exponential case, the temperature dependence of both terms is reduced because $E_{F,h}$ does not depend explicitly on temperature.

These trends are indeed observed in the experimental $V_{OC}(T)$ data plotted in **Figure 5**a. Not only is the V_{OC} higher for PM6:Y6, due to smaller disorder, but it also displays a steeper slope of the $V_{OC}(T)$ dependence at higher temperatures. For low temperatures, the temperature dependence of V_{OC} becomes smaller for both systems, indicating the transition to the degenerate

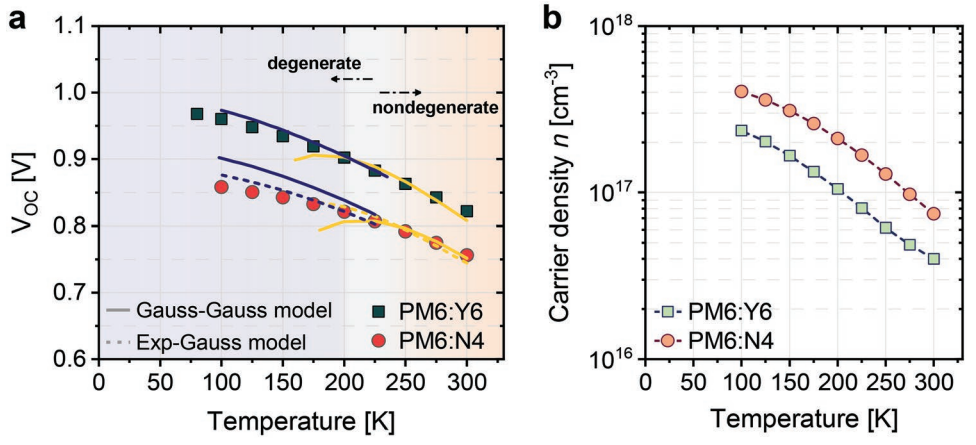

Figure 5. a) Open-circuit voltage V_{OC} as a function of temperature for PM6:Y6 and PM6:N4 devices (full symbols). The experimental data were fitted according to the Gaussian–Gaussian model (full lines) or the Gaussian-exponential model (dashed lines) using the expressions in the non-degenerate and degenerate regions, with the transition marked between 200 and 250 K depending on the blend and charge carrier density. The fitting parameters can be found in Table S3 (Supporting Information). b) Temperature dependence of the charge carrier density n for the blends PM6:Y6 and PM6:N4 devices (symbols), obtained via PIA. Dashed lines are a guide to the eye.

regime. The analytical description of the experimental $V_{OC}(T)$ data requires knowledge of the temperature-dependent carrier density. Determination of n at low temperatures with BACE is problematic as this method relies on the extraction of charges. We have therefore applied PIA spectroscopy, which is an extraction-less technique, with the results shown in Figure 5b for 1 sun illumination conditions. First, we observe that the carrier density n is consistently higher in PM6:N4, in agreement with the smaller k_2 reported above. More importantly, for both blends there is an increase of n over the entire temperature range, being stronger at first from 300 to 200 K.

With $n(T)$ at hand, we are now in a position to analytically describe the progression of the V_{OC} with temperature (Figure 5a). For PM6:Y6 with two Gaussian distributions, $V_{OC}(T)$ was fitted with a combination of Equation (3a); and Equation S3e (Supporting Information); see Note S4 (Supporting Information for the discussion of the applicability of the equations. The fitting parameters are collected in Table S3 (Supporting Information). N_0 was set to the number density of Y6/N4 molecules in the blend ($N_{Y6/N4} = 2.4 \times 10^{20}$ cm^{-3})[55] and the values of $\sigma_{L,A}$ and $\sigma_{H,D}$ were fixed as obtained from SCLC, leaving the HOMO–LUMO gap as the only free parameter. As shown by the solid lines in Figure 5a, this approach explains well the temperature dependence of V_{OC}, yielding a reasonable value for the bandgap, $E_g = 1.42 \pm 0.15$ eV. Notably, when the system has fully entered the degenerate regime, the temperature does not appear as an independent variable anymore but influences V_{OC} only through the temperature dependence of the carrier density. Therefore, without knowledge of $n(T)$, the analysis of $V_{OC}(T)$ will likely lead to wrong conclusions. We note a small discontinuity of the predicted $V_{OC}(T)$ from Equation (3a); and Equation S3e (Supporting Information) at the transition from the non-degenerate to the degenerate regions at around 200 K. The reason is that Equation (3a) becomes inaccurate at this transition, but unfortunately, there is no analytical approximation to provide a description of the entire transition region. For the same reason, the bandgap from the fit is slightly different for the high and low temperature regimes.

The fit to the PM6:N4 device with the Gaussian–Gaussian model and the disorder values deduced from SCLC works well in the non-degenerate regime, but the model fails to explain the data in the low temperature region, where it predicts a stronger temperature dependence (Figure 5a). In contrast, the Gaussian-exponential model (Equation (3b); and Equation (S3f), Supporting Information), marked in the plot with dashed lines, reproduces the V_{OC} over the entire temperature range. As detailed above, the lack of a temperature dependence of the (quasi-)Fermi level causes a smaller dependence of the V_{OC} on temperature, exactly as we observe in the PM6:N4 experimental data. The data could be well fitted using $T_0 = 435$ K, the value predicted from the m(T) and n_{id}(T) data (Figure 4a). We notice that the V_{OC} does not increase as much as the models would predict toward lower temperatures, in neither PM6:Y6 and PM6:N4 devices. To ensure that the reduction of the V_{OC} is not a consequence of high leakage current,[75] we compared the light and dark J–Vs in Figure S15 (Supporting Information). The dark current decreases with temperature, and it is much lower than the photocurrent at low temperatures. For both systems, at 100 K, subtracting the leakage current from the photocurrent increases the V_{OC} by less than 5 mV, thus we conclude that the leakage effect is negligible. Another potential source of V_{OC} saturation is a low built-in voltage, e.g., due to a too small difference between the electrodes or an injection barrier.[20,76,77] We, therefore, measured $V_{OC}(T)$ for different illumination intensities (Figure S16, Supporting Information). Instead of converging towards a fixed V_{OC}, changing the intensity leads to a horizontal shift of the $V_{OC}(T)$, with little distortion of the shape. In fact, we could reproduce the entire data set with the parameters determined from the fit to the 1 sun $V_{OC}(T)$ data and assuming that recombination is bimolecular for all temperatures (the carrier density depends strictly on the square root of the intensity). We, therefore, believe that the slight deviation of the measured and predicted V_{OC} at low temperatures has other reasons. We, finally, point out that all published $V_{OC}(T)$ data for the PM6:Y6 blend exhibit very similar behavior, implying that the underlying phenomena are intrinsic to the blend.

3. Discussion

Our data show that energetic disorder has a pronounced effect on the absolute value of the V_{OC} but also on the steepness of its temperature dependence, already at room temperature. Consequently, disorder affects the interpretation of the linear extrapolation of the $V_{OC}(T)$ to $T = 0$, which is typically assigned to the energy of the recombining state; the charge transfer (CT) state (in organic solar cells). For PM6:Y6, the extrapolation gives $qV_{OC}(T = 0\ \text{K}) \cong 1.1$ eV. Because of the strong contribution of the NFA singlet excitons to the absorption and emission of this blend, there is yet no accurate value of the CT energy of PM6:Y6. Moreover, because of the energetic disorder, the mean energy of the populated CT state manifold is itself a function of temperature and referring to one CT state energy is meaningless.[78,79] The situation is similar for PM6:N4, where $qV_{OC}(T = 0\ \text{K}) \cong 1.0$ eV is an unreasonably low value. Therefore, the extrapolation of qV_{OC} will not provide a reasonable estimate of the mean energy of the CT state manifold in these blends.

For PM6:Y6, the temperature-dependent charge transport can be consistently described by a Gaussian-type donor HOMO and acceptor LUMO, with a width of 74 and 60 meV, respectively. This picture is confirmed by the recombination analysis, which yielded n_{id} and m independent of temperature and close to one. Importantly, the very same disorder parameters deduced from transport measurements explain the course of the temperature-dependent V_{OC}. It has been proposed that OSCs are non-equilibrium hot carrier devices, where photogenerated carriers leave the device before they equilibrate in the DOS.[31,32] While there is consistent proof that hot carriers assist charge extraction for highly disordered blends,[80] there is a current debate whether the same mechanism is functional at open-circuit conditions.[28] Very recently, kinetic Monte Carlo (kMC) simulations on a PM6:Y6 blend suggested a 130 meV increase in V_{OC} compared to the case of fully equilibrated charges.[81] It was also suggested that photogenerated charge carriers exit the device via one of the contacts, followed by reinjection and recombination of equilibrated charge. While we cannot fully rule out that nonequilibrated carriers affect the measured V_{OC} in our devices, we argue that experiments on PM6:Y6 blends without and with electrodes

gave the same recombination rate.[53] Also, our steady-state approach reproduces the $V_{OC}(T)$ on the basis of the measured carrier densities and disorders, for different illumination intensities, with the HOMO–LUMO splitting as the only unknown parameter. We see this as a strong proof that the QFLS and with that the V_{OC} is mostly determined by equilibrated carriers.

For the PM6:N4 blend, the combination of two Gaussians yields a good prediction for $V_{OC}(T)$ at higher temperatures but does not provide a good fit of the low temperature regime. Here, the combination of a Gaussian-shaped N4 LUMO with a broader PM6 HOMO that has an exponential tail gives a much better description. Again, we find a very similar dependence of the carrier density on fluence for the neat PM6:N4 film and device (Figure S5, Supporting Information), meaning that the recombination properties are not affected by the presence of the electrodes. It is, however, unlikely that the replacement of Y6 by N4 transforms the entire PM6 HOMO into an exponential DOS. Rather than that, we presume that the larger distortion of the PM6 phase in the PM6:N4 blend but also the mixing of N4 molecules into the polymer phase broadens the tail of the DOS. As N4 and Y6 have the same conjugated core, we expect the same electric dipole and quadrupole moment for both molecules. It has been shown that a small concentration of randomly oriented electric dipoles creates a Lorentzian DOS.[58] Similarly, a random distribution of point charges creates exponential band tails.[59] Such tail broadening has been experimentally observed in doped organic molecules and polymers.[82] Further experiments and simulations are needed to reveal the true origin and shape of the PM6 HOMO, which is however beyond the scope of this paper. As a side note, such nonuniform DOS explains why T_0 from the analysis of the SCLC transport is different from the value extracted from the recombination studies. The reason is that the SCLC current is proportional to the density of free charges while, in our model, the recombination concerns mainly charges in the tail of the distribution.

The lower V_{OC} of the PM6:N4 blend is consistent with a picture of equilibrated charges in a broader density of states distribution. This raises the questions whether a similar broadening concerns the CT state manifold. Because of additional disorder of the electrostatic interaction, it is predicted that the distribution of the CT energies is wider than that of the charge-separated states.[83] Also, the larger morphological disorder at the donor–acceptor interface would potentially broaden the CT DOS.[29] Unfortunately, the presence of a strong absorption and emission from Y6 excitons prevents the determination of the spectral position and width of the CT emission in PM6:Y6.[55] In EL measurements, this is observed by injected free charges that are reformed into singlet excitons. Figure S17 (Supporting Information) shows the EL spectra of a PM6:N4 device as a function of temperature. At 300 K, the peak at 1.32 eV corresponds to the N4 singlet but we observe that, as the sample is cooled down, a low energy contribution becomes discernible. The peak is at 1.10 eV at 300 K and it overcomes the singlet below 240 K. This is different in PM6:Y6, where the low energy peak is at ≈1.15 eV at 300 K, but the singlet emission dominates at all temperatures.[55] For both cases, the intensity of the low energy emission is independent of temperature for a given injection current, implying that it originates from the radiative recombination of the main recombining state–the CT state. These results point to a lower energy of the populated CT manifold in PM6:N4, e.g., due to an overall lower CT energy or by more pronounced state broadening. Energetic disorder is indicated by the redshift of the low energy emission peak in Figure S17 (Supporting Information) with decreasing temperature. With respect to this, recent kMC simulations suggested that free charge encounter forms an athermal CT population, whose mean energy is not simply determined by the CT state properties but in addition by the energy of the encountering charges, which itself is a function of temperature.[84] Irrespective of the exact mechanism, the data show that for PM6:N4, the offset between the populated CT and singlet state is larger, which explains the lower contribution by singlet emission and why the ELQY is more than one order of magnitude lower in PM6:N4 compared to PM6:Y6 (Figure S3, Supporting Information). This, in turn, explains the nonradiative voltage losses in PM6:N4.

Finally, we find that the free carrier density increases with decreasing temperature in both blends. At V_{OC}, CT states and free carriers (in the charge-separated, CS, state) are in dynamic equilibrium.[85] Our data suggest that the CT-CS balance shifts toward free charges for a lower T. In other words, the reformation of CT states by free charge encounter is more affected by the lowering of the temperature than the redissociation of these states into free charges. Recent transient absorption and time-resolved photoluminescence experiments suggested that charges in PM6:Y6 have to overcome a substantial Coulomb-barrier to form free carriers, which would favor CT reformation at lower temperatures.[86] On the other hand, recent simulations showed that this barrier due to mutual Coulomb attraction can be fully compensated by strong band bending across the D:A heterojunction.[87] Energetic disorder will add complexity to these models as it provides additional low-lying states to host free charges.[88,89] From the parameters deduced above, we conclude that the mean energy of the populated CS states is never larger than 1.1 eV in PM6:Y6 (see the Note S4 and Figure S14, Supporting Information). This is significantly smaller than the Y6 singlet energy and, according to the EL spectra, lower than the populated CT energy. As such, energetic disorder is likely to contribute to free charge formation in such high-performance NFA-based blends.

4. Conclusion

In summary, by comparing the temperature-dependent charge transport and recombination properties of PM6 blended with two Y-series NFAs, Y6, and N4, we show that energetic disorder plays an important role even in high-efficiency organic solar cells. Studies of the blend morphology reveal a different packing and larger structural disorder in the PM6:N4 blend, which translates into a larger energetic disorder but also different shape of the density of states distributions. This is confirmed by temperature-dependent BACE and *JV* measurements, which reveal that the blends exhibit different nongeminate recombination mechanism: in PM6:Y6, recombination occurs between carriers in two rather narrow Gaussian state distributions, while in PM6:N4, recombination is predominantly between carriers in a Gaussian-shaped LUMO DOS with carriers in the tail of a broader HOMO DOS with a more exponential character. This information combined with the carrier densities from photoinduced

absorption allows us to analytically describe the V_{OC} as a function of temperature and illumination intensity. Hereby, we find that the free carrier density increases with decreasing temperatures in both PM6:Y6 and PM6:N4, indicative of a down-hill driving force for free charge formation assisted by energetic disorder. Regarding the CT properties, electroluminescence measurements reveal a red-shifted CT emission in PM6:N4 compared to PM6:Y6, which becomes predominant over the singlet at low temperatures. This points to a lower energy of the populated CT state manifold, possibly due to a wider distribution of the CT energies in this more disordered blend, which goes along with a larger nonradiative voltage loss in PM6:N4. We conclude that energetic disorder has to be taken into account when considering the absolute value of the V_{OC} but also the steepness of its temperature dependence, and that the treatment of recombination and related properties with single CT and charge transporting levels is inappropriate. In this regard, PM6:Y6 benefits substantially from a narrower Gaussian-type density of state distribution, giving promise for the development of NFA-based solar cells with even smaller V_{OC} losses once the origin of energetic disorder is properly understood.

Supporting Information

Supporting Information is available from the Wiley Online Library or from the author.

Acknowledgements

This work has been funded by the Alexander von Humboldt Foundation (Sofja Kovalewskaja-Award) and from the Deutsche Forschungsgemeinschaft, DFG, German Research Foundation through the project Fabulous (project number 450968074) and HIOS (project number 182087777 – SFB 951), as well as project number 3923306670. E.M.H. and F.E. acknowledge funding from SolarEraNet (No. NFA4R2ROPV). F.E. thanks the Elite Study Program Macromolecular Science within the Elite Network of Bavaria (ENB) for support. This research used the Soft Matter Interfaces Beamline (SMI, Beamline 12-ID) of the National Synchrotron Light Source II, a U.S. Department of Energy (DOE) Office of Science User Facility operated for the DOE Office of Science by Brookhaven National Laboratory under Contract No. DE-SC0012704. This publication is based upon work supported by the King Abdullah University of Science and Technology (KAUST) Office of Sponsored Research (OSR) under Award No: OSR-CARF/CCF-3079. Q.W. and Y.Z. acknowledge National Natural Science Foundation of China (No. 52125306). A.A. acknowledges support from the Welsh Government's Sêr Cymru II Rising Star and Capacity Builder Accelerator Programs through the European Regional Development Fund, Welsh European Funding Office, and Swansea University Strategic Initiative in Sustainable Advanced Materials.

Open access funding enabled and organized by Projekt DEAL.

Conflict of Interest

The authors declare no conflict of interest.

Data Availability Statement

The data that support the findings of this study are available from the corresponding author upon reasonable request.

Keywords

energetic disorder, non-fullerene acceptors, open-circuit voltage, organic solar cells

Received: November 2, 2021
Revised: December 11, 2021
Published online:

[1] A. Armin, W. Li, O. J. Sandberg, Z. Xiao, L. Ding, J. Nelson, D. Neher, K. Vandewal, S. Shoaee, T. Wang, H. Ade, T. Heumüller, C. Brabec, P. Meredith, *Adv. Energy Mater.* **2021**, *11*, 2003570.
[2] Q. Liu, Y. Jiang, K. Jin, J. Qin, J. Xu, W. Li, J. Xiong, J. Liu, Z. Xiao, K. Sun, S. Yang, X. Zhang, L. Ding, *Sci. Bull.* **2020**, *65*, 272.
[3] Y. Cui, H. Yao, J. Zhang, K. Xian, T. Zhang, L. Hong, Y. Wang, Y. Xu, K. Ma, C. An, C. He, Z. Wei, F. Gao, J. Hou, *Adv. Mater.* **2020**, *32*, 1908205.
[4] Y. Lin, Y. Firdaus, F. H. Isikgor, M. I. Nugraha, E. Yengel, G. T. Harrison, R. Hallani, A. El-Labban, H. Faber, C. Ma, X. Zheng, A. Subbiah, C. T. Howells, O. M. Bakr, I. McCulloch, S. De Wolf, L. Tsetseris, T. D. Anthopoulos, *ACS Energy Lett.* **2020**, *5*, 2935.
[5] T. Zhang, C. An, P. Bi, Q. Lv, J. Qin, L. Hong, Y. Cui, S. Zhang, J. Hou, *Adv. Energy Mater.* **2021**, *11*, 2101705.
[6] F. Liu, L. Zhou, W. Liu, Z. Zhou, Q. Yue, W. Zheng, R. Sun, W. Liu, S. Xu, H. Fan, L. Feng, Y. Yi, W. Zhang, X. Zhu, *Adv. Mater.* **2021**, *33*, 2100830.
[7] J. Yuan, Y. Zhang, L. Zhou, G. Zhang, H.-L. Yip, T.-K. Lau, X. Lu, C. Zhu, H. Peng, P. A. Johnson, M. Leclerc, Y. Cao, J. Ulanski, Y. Li, Y. Zou, *Joule* **2019**, *3*, 1140.
[8] L. Perdigón-Toro, H. Zhang, A. Markina, J. Yuan, S. M. Hosseini, C. M. Wolff, G. Zuo, M. Stolterfoht, Y. Zou, F. Gao, D. Andrienko, S. Shoaee, D. Neher, *Adv. Mater.* **2020**, *32*, 1906763.
[9] G. Zhang, X. K. Chen, J. Xiao, P. C. Y. Chow, M. Ren, G. Kupgan, X. Jiao, C. C. S. Chan, X. Du, R. Xia, Z. Chen, J. Yuan, Y. Zhang, S. Zhang, Y. Liu, Y. Zou, H. Yan, K. S. Wong, V. Coropceanu, N. Li, C. J. Brabec, J. L. Bredas, H. L. Yip, Y. Cao, *Nat. Commun.* **2020**, *11*, 3943.
[10] L. Zhu, M. Zhang, G. Zhou, T. Hao, J. Xu, J. Wang, C. Qiu, N. Prine, J. Ali, W. Feng, X. Gu, Z. Ma, Z. Tang, H. Zhu, L. Ying, Y. Zhang, F. Liu, *Adv. Energy Mater.* **2020**, *10*, 1904234.
[11] Z. Bi, K. Chen, L. Gou, Y. Guo, X. Zhou, H. B. Naveed, J. Wang, Q. Zhu, J. Yuan, C. Zhao, K. Zhou, S. Chandrabose, Z. Tang, Y. Yi, J. M. Hodgkiss, L. Zhang, W. Ma, *J. Mater. Chem. A* **2021**, *9*, 16733.
[12] G. Kupgan, X. K. Chen, J. L. Brédas, *Mater. Today Adv.* **2021**, *11*, 100154.
[13] N. Tokmoldin, J. Vollbrecht, S. M. Hosseini, B. Sun, L. Perdigón-Toro, H. Y. Woo, Y. Zou, D. Neher, S. Shoaee, *Adv. Energy Mater.* **2021**, *11*, 2100804.
[14] J. Wu, J. Lee, Y. C. Chin, H. Yao, H. Cha, J. Luke, J. Hou, J. S. Kim, J. R. Durrant, *Energy Environ. Sci.* **2020**, *13*, 2422.
[15] S. M. Hosseini, N. Tokmoldin, Y. W. Lee, Y. Zou, H. Y. Woo, D. Neher, S. Shoaee, *Sol. RRL* **2020**, *4*, 2000498.
[16] H. Bässler, *Phys. Status Solidi* **1993**, *175*, 15.
[17] S. D. Baranovskii, *Phys. Status Solidi* **2014**, *251*, 487.
[18] A. Hofacker, J. O. Oelerich, A. V. Nenashev, F. Gebhard, S. D. Baranovskii, *J. Appl. Phys.* **2014**, *115*, 223713.
[19] V. Coropceanu, J. L. Brédas, S. Mehraeen, *J. Phys. Chem. C* **2017**, *121*, 24954.
[20] J. C. Blakesley, D. Neher, *Phys. Rev. B* **2011**, *84*, 075210.
[21] D. Credgington, J. R. Durrant, *J. Phys. Chem. Lett.* **2012**, *3*, 1465.
[22] S. D. Collins, C. M. Proctor, N. A. Ran, T.-Q. Nguyen, *Adv. Energy Mater.* **2016**, *6*, 1501721.
[23] A. Foertig, A. Baumann, D. Rauh, V. Dyakonov, C. Deibel, *Appl. Phys. Lett.* **2009**, *95*, 052104.

[24] G. Garcia-Belmonte, J. Bisquert, *Appl. Phys. Lett.* **2010**, *96*, 113301.
[25] T. Kirchartz, B. E. Pieters, J. Kirkpatrick, U. Rau, J. Nelson, *Phys. Rev. B* **2011**, *83*, 115209.
[26] F. Etzold, I. A. Howard, R. Mauer, M. Meister, T. D. Kim, K. S. Lee, N. S. Baek, F. Laquai, *J. Am. Chem. Soc.* **2011**, *133*, 9469.
[27] T. Kirchartz, J. Nelson, *Phys. Rev. B* **2012**, *86*, 165201.
[28] S. Roland, J. Kniepert, J. A. Love, V. Negi, F. Liu, P. Bobbert, A. Melianas, M. Kemerink, A. Hofacker, D. Neher, *J. Phys. Chem. Lett.* **2019**, *10*, 1374.
[29] W. Kaiser, A. Gagliardi, *J. Phys. Chem. Lett.* **2019**, *10*, 6097.
[30] A. Melianas, V. Pranculis, A. Devižis, V. Gulbinas, O. Inganäs, M. Kemerink, *Adv. Funct. Mater.* **2014**, *24*, 4507.
[31] A. Melianas, F. Etzold, T. J. Savenije, F. Laquai, O. Inganäs, M. Kemerink, *Nat. Commun.* **2015**, *6*, 8778.
[32] A. Melianas, V. Pranculis, Y. Xia, N. Felekidis, O. Inganäs, V. Gulbinas, M. Kemerink, *Adv. Energy Mater.* **2017**, *7*, 1602143.
[33] T. Upreti, Y. Wang, H. Zhang, D. Scheunemann, F. Gao, M. Kemerink, *Phys. Rev. Appl.* **2019**, *12*, 064039.
[34] J. Kurpiers, T. Ferron, S. Roland, M. Jakoby, T. Thiede, F. Jaiser, S. Albrecht, S. Janietz, B. A. Collins, I. A. Howard, D. Neher, *Nat. Commun.* **2018**, *9*, 2038.
[35] N. R. Tummala, S. Mehraeen, Y. T. Fu, C. Risko, J. L. Brédas, *Adv. Funct. Mater.* **2013**, *23*, 5800.
[36] N. R. Tummala, Z. Zheng, S. G. Aziz, V. Coropceanu, J. L. Brédas, *J. Phys. Chem. Lett.* **2015**, *6*, 3657.
[37] H. Cha, Y. Zheng, Y. Dong, H. H. Lee, J. Wu, H. Bristow, J. Zhang, H. K. H. Lee, W. C. Tsoi, A. A. Bakulin, I. McCulloch, J. R. Durrant, *Adv. Energy Mater.* **2020**, *10*, 2001149.
[38] S. Liu, J. Yuan, W. Deng, M. Luo, Y. Xie, Q. Liang, Y. Zou, Z. He, H. Wu, Y. Cao, *Nat. Photonics* **2020**, *14*, 300.
[39] J. Yuan, C. Zhang, H. Chen, C. Zhu, S. H. Cheung, B. Qiu, F. Cai, Q. Wei, W. Liu, H. Yin, R. Zhang, J. Zhang, Y. Liu, H. Zhang, W. Liu, H. Peng, J. Yang, L. Meng, F. Gao, S. So, Y. Li, Y. Zou, *Sci. China Chem.* **2020**, *63*, 1159.
[40] A. Hofacker, D. Neher, *Phys. Rev. B* **2017**, *96*, 245204.
[41] S. Xie, Y. Xia, Z. Zheng, X. Zhang, J. Yuan, H. Zhou, Y. Zhang, *Adv. Funct. Mater.* **2018**, *28*, 1705659.
[42] V. V. Brus, N. Schopp, S. Ko, J. Vollbrecht, J. Lee, A. Karki, G. C. Bazan, T. Nguyen, *Adv. Energy Mater.* **2021**, *11*, 2003091.
[43] C. He, Y. Li, Y. Liu, Y. Li, G. Zhou, S. Li, H. Zhu, X. Lu, F. Zhang, C. Z. Li, H. Chen, *J. Mater. Chem. A* **2020**, *8*, 18154.
[44] C. Zhang, J. Yuan, K. L. Chiu, H. Yin, W. Liu, G. Zheng, J. K. W. Ho, S. Huang, G. Yu, F. Gao, Y. Zou, S. K. So, *J. Mater. Chem. A* **2020**, *8*, 8566.
[45] C. Kaiser, O. J. Sandberg, N. Zarrabi, W. Li, P. Meredith, A. Armin, *Nat. Commun.* **2021**, *12*, 3988.
[46] A. Karki, J. Vollbrecht, A. J. Gillett, S. S. Xiao, Y. Yang, Z. Peng, N. Schopp, A. L. Dixon, S. Yoon, M. Schrock, H. Ade, G. N. M. Reddy, R. H. Friend, T. Q. Nguyen, *Energy Environ. Sci.* **2020**, *13*, 3679.
[47] P. Wan, X. Chen, Q. Liu, S. Mahadevan, M. Guo, J. Qiu, X. Sun, S.-W. Tsang, M. Zhang, Y. Li, S. Chen, *J. Phys. Chem. Lett.* **2021**, *12*, 10595.
[48] K. Jiang, Q. Wei, J. Y. L. Lai, Z. Peng, H. K. Kim, J. Yuan, L. Ye, H. Ade, Y. Zou, H. Yan, *Joule* **2019**, *3*, 3020.
[49] S. Li, C.-Z. Li, M. Shi, H. Chen, *ACS Energy Lett.* **2020**, *5*, 1554.
[50] J. Kniepert, I. Lange, N. J. van der Kaap, L. J. A. Koster, D. Neher, *Adv. Energy Mater.* **2014**, *4*, 1301401.
[51] S. M. Hosseini, S. Roland, J. Kurpiers, Z. Chen, K. Zhang, F. Huang, A. Armin, D. Neher, S. Shoaee, *J. Phys. Chem. C* **2019**, *123*, 6823.
[52] L. Quang Phuong, S. Mehrdad Hosseini, C. Woo Koh, H. Young Woo, S. Shoaee, *J. Phys. Chem. C* **2019**, *123*, 27417.
[53] L. Q. Phuong, S. M. Hosseini, O. J. Sandberg, Y. Zou, H. Y. Woo, D. Neher, S. Shoaee, *Sol. RRL* **2020**, *5*, 2000649.
[54] J. Kniepert, A. Paulke, L. Perdigón-Toro, J. Kurpiers, H. Zhang, F. Gao, J. Yuan, Y. Zou, V. M. Le Corre, L. J. A. Koster, D. Neher, *J. Appl. Phys.* **2019**, *126*, 205501.
[55] L. Perdigón-Toro, L. Quang Phuong, S. Zeiske, K. Vandewal, A. Armin, S. Shoaee, D. Neher, *ACS Energy Lett.* **2021**, *6*, 557.
[56] S. Dong, T. Jia, K. Zhang, J. Jing, F. Huang, *Joule* **2020**, *4*, 2004.
[57] L. Hong, H. Yao, Z. Wu, Y. Cui, T. Zhang, Y. Xu, R. Yu, Q. Liao, B. Gao, K. Xian, H. Y. Woo, Z. Ge, J. Hou, *Adv. Mater.* **2019**, *31*, 1903441.
[58] A. Dieckmann, H. Bässler, P. M. Borsenberger, *J. Chem. Phys.* **1993**, *99*, 8136.
[59] M. Silver, L. Pautmeier, H. Bässler, *Solid State Commun.* **1989**, *72*, 177.
[60] K. Vandewal, J. Widmer, T. Heumueller, C. J. Brabec, M. D. McGehee, K. Leo, M. Riede, A. Salleo, *Adv. Mater.* **2014**, *26*, 3839.
[61] A. Zusan, K. Vandewal, B. Allendorf, N. H. Hansen, J. Pflaum, A. Salleo, V. Dyakonov, C. Deibel, *Adv. Energy Mater.* **2014**, *4*, 1400922.
[62] U. Rau, *Phys. Rev. B: Condens. Matter Mater. Phys.* **2007**, *76*, 085303.
[63] N. I. Craciun, J. J. Brondijk, P. W. M. Blom, *Phys. Rev. B: Condens. Matter Mater. Phys.* **2008**, *77*, 035206.
[64] N. Felekidis, A. Melianas, M. Kemerink, *Org. Electron.* **2018**, *61*, 318.
[65] G. Zuo, Z. Li, O. Andersson, H. Abdalla, E. Wang, M. Kemerink, *J. Phys. Chem. C* **2017**, *121*, 7767.
[66] G. Zuo, M. Linares, T. Upreti, M. Kemerink, *Nat. Mater.* **2019**, *18*, 588.
[67] P. W. M. Blom, M. J. M. de Jong, J. J. M. Vleggaar, *Appl. Phys. Lett.* **1996**, *63*, 3308.
[68] R. Steyrleuthner, S. Bange, D. Neher, *J. Appl. Phys.* **2009**, *105*, 064509.
[69] G. A. H. Wetzelaer, M. Kuik, H. T. Nicolai, P. W. M. Blom, *Phys. Rev. B: Condens. Matter Mater. Phys.* **2011**, *83*, 165204.
[70] D. Rauh, C. Deibel, V. Dyakonov, *Adv. Funct. Mater.* **2012**, *22*, 3371.
[71] T. Ripolles-Sanchis, S. R. Raga, A. Guerrero, M. Welker, M. Turbiez, J. Bisquert, G. Garcia-Belmonte, *J. Phys. Chem. C* **2013**, *117*, 8719.
[72] G. Paasch, S. Scheinert, *J. Appl. Phys.* **2010**, *107*, 104501.
[73] N. Zarrabi, O. J. Sandberg, S. Zeiske, W. Li, D. B. Riley, P. Meredith, A. Armin, *Nat. Commun.* **2020**, *11*, 5567.
[74] P. Mark, W. Helfrich, *J. Appl. Phys.* **1962**, *33*, 205.
[75] Y. Tang, J. M. Bjuggren, Z. Fei, M. R. Andersson, M. Heeney, C. R. McNeill, *Sol. RRL* **2020**, *4*, 2000375.
[76] F. Gao, W. Tress, J. Wang, O. Inganäs, *Phys. Rev. Lett.* **2015**, *114*, 128701.
[77] A. Spies, M. List, T. Sarkar, U. Würfel, *Adv. Energy Mater.* **2017**, *7*, 1601750.
[78] T. M. Burke, S. Sweetnam, K. Vandewal, M. D. McGehee, *Adv. Energy Mater.* **2015**, *5*, 1500123.
[79] J. Yan, E. Rezasoltani, M. Azzouzi, F. Eisner, J. Nelson, *Nat. Commun.* **2021**, *12*, 3642.
[80] N. Gasparini, M. Salvador, T. Heumueller, M. Richter, A. Classen, S. Shrestha, G. J. Matt, S. Holliday, S. Strohm, H.-J. Egelhaaf, A. Wadsworth, D. Baran, I. McCulloch, C. J. Brabec, *Adv. Energy Mater.* **2017**, *7*, 1701561.
[81] T. Upreti, S. Wilken, H. Zhang, M. Kemerink, *J. Phys. Chem. Lett.* **2021**, *12*, 9874.
[82] P. Pingel, D. Neher, *Phys. Rev. B: Condens. Matter Mater. Phys.* **2013**, *87*, 115209.
[83] Z. Zheng, N. R. Tummala, T. Wang, V. Coropceanu, J. Brédas, *Adv. Energy Mater.* **2019**, *9*, 1803926.
[84] G. Zuo, S. Shoaee, M. Kemerink, D. Neher, *Phys. Rev. Appl.* **2021**, *16*, 034027.
[85] O. J. Sandberg, A. Armin, *J. Phys. Chem. C* **2021**, *125*, 15590.

[86] C. C. S. Chan, C. Ma, X. Zou, Z. Xing, G. Zhang, H. Yip, R. A. Taylor, Y. He, K. S. Wong, P. C. Y. Chow, *Adv. Funct. Mater.* **2021**, *31*, 2107157.
[87] S. Karuthedath, J. Gorenflot, Y. Firdaus, N. Chaturvedi, C. S. P. De Castro, G. T. Harrison, J. I. Khan, A. Markina, A. H. Balawi, T. A. Dela Peña, W. Liu, R. Z. Liang, A. Sharma, S. H. K. Paleti, W. Zhang, Y. Lin, E. Alarousu, D. H. Anjum, P. M. Beaujuge, S. De Wolf, I. McCulloch, T. D. Anthopoulos, D. Baran, D. Andrienko, F. Laquai, *Nat. Mater.* **2020**, *20*, 378.
[88] S. N. Hood, I. Kassal, *J. Phys. Chem. Lett.* **2016**, *7*, 4495.
[89] S. Athanasopoulos, H. Bässler, A. Köhler, *J. Phys. Chem. Lett.* **2019**, *10*, 7107.